The Astrophysical Journal, 890:50 (14pp), 2020 February 10 https://doi.org/10.3847/1538-4357/ab61fa

Space Velocity and Time Span of Jets in Planetary Nebulae

Martín A. Guerrero[1], Jackeline Suzett Rechy-García[1,2], and Roberto Ortiz[3]
[1] Instituto de Astrofísica de Andalucía, IAA-CSIC Glorieta de la Astronomía s/n, E-18008 Granada, Spain; mar@iaa.es
[2] Instituto de Astronomía, Universidad Nacional Autónoma de México Apdo. Postal 70264, 04510, Ciudad de México, Mexico
[3] Escola de Artes, Ciências e Humanidades, USP Av. Arlindo Bettio 1000, 03828-000 São Paulo, Brazil
Received 2019 July 10; revised 2019 November 30; accepted 2019 December 13; published 2020 February 12

Abstract

Fast highly collimated outflows, including bipolar knots, jetlike features, and point-symmetric filaments or strings of knots, are common in planetary nebulae (PNe). These features, generally known as jets, are thought to play an active role in the nebular shaping immediately before or while fast stellar winds and D-type ionization fronts shock and sweep up the nebular envelope. The space velocity, radial distance from the central star, and kinematic age of the jets in PNe cannot be determined because the inclination angle with the line of sight is usually unknown. Here we have used the large number of jets already detected in PNe to derive orientation-independent properties from a statistical point of view. We find that jets in PNe can be assigned to two different populations: most (about 70%) have space velocities below 100 km s^{-1}, and only 30% have larger velocities. Since a significant fraction of jets move at velocities similar to that of their parent PNe and are found close to the nebular edge, we propose that these jets have been slowed down in their interaction with the nebular envelope, contributing to the expansion of their PNe. The time spans before the jets dissolve are found to be generally shorter than 2500 yr. Since most jets are found in young PNe of similar (1000–3000 yr) age, it can be concluded that jets are mostly coeval with their PNe.

Unified Astronomy Thesaurus concepts: Planetary nebulae (1249); Jets (870); Circumstellar envelopes (237); Late stellar evolution (911)

1. Introduction

A fraction of planetary nebulae (PNe) present morphological and kinematic features indicative of fast and highly collimated outflows. These are mostly detected in narrowband images (e.g., Corradi et al. 1996) as low-ionization features with a variety of morphologies, including jetlike features, bipolar compact knots, and point-symmetric filamentary structures or strings of knots. Such morphological variety has made researchers coin a number of names to designate them, including bipolar rotating episodic jets (BRETs; López et al. 1995), fast low-ionization emission regions (FLIERs; Balick et al. 1993), or simply jets. Hereafter, we adopt the latter term to refer to them, despite their morphological diversity. Kinematically, they are characterized by anomalous radial velocities with respect to the velocity field of the PN and narrow, unresolved velocity structures.

Jets are found in PNe spanning almost all morphological classes (Guerrero et al. 1999; Gonçalves et al. 2001) and evolutionary stages (Bond & Livio 1990; Alcolea et al. 2000; Cox et al. 2000; Goldman et al. 2004). It is nowadays commonly accepted that jets play a critical role in the shaping of axisymmetric PNe (Sahai & Trauger 1998), although the first detection of such a fast collimated outflow in a PN, namely NGC 2392 (Gieseking et al. 1985), was completely unexpected because it was unforeseen that progenitor stars of PNe could host accretion disks and/or have strong magnetic fields to provide the required conditions for the collimation and acceleration of a jet (Livio 1999). Different models have been proposed to explain the formation of jets in PNe, including hydrodynamical focusing (Frank et al. 1996), magnetic collimation (García-Segura 1997), and accretion disks (Morris 1987; Soker & Livio 1994), but none of them offer a comprehensive explanation of all their properties (Balick et al. 1998; Gonçalves et al. 2001).

Most observational studies of jets report the spatial and kinematic properties in one single object or a small sample of sources (e.g., Balick et al. 1987; Miranda & Solf 1992; Lopez et al. 1993; Guerrero et al. 1999; Corradi et al. 2000; Akras & López 2012, among many others). Only a few studies have dealt with averaged properties for a sample of PNe, considering the morphological and kinematic properties (Gonçalves et al. 2001; Akras & Gonçalves 2016) or the linear momenta of the jets (Tocknell et al. 2014). The real space velocity of a jet could provide basic insights on its formation mechanisms and interactions with the nebular envelope, but it is unknown due to projection effects because the angle between the velocity vector and the line of sight cannot be determined. Only in a few cases is there some additional information that can be used to constrain the real space velocity. The width of the line at zero intensity, FWZI, is a direct measurement of the real space velocity (Hartigan et al. 1987). Unfortunately, this procedure requires a high signal-to-noise ratio in order to determine the zero-intensity level accurately. More frequently, the real space velocity of the collimated outflow is worked out after a spatiokinematic model has been built for the main nebula (e.g., Clark et al. 2010) or for multiple ejecta located at different orientations (e.g., Miranda et al. 1999), or the shock velocity is derived from suitable spectral diagnostics (e.g., Guerrero et al. 2004). This requires adopting simple assumptions on the geometry and kinematics of the jets and their relation to different nebular structures.

In this paper, we present an analysis of the spatial and kinematic properties of a sample of jets in PNe using a statistical approach. The observed distributions of radial velocity and distance to the central star (CSPN) projected on the plane of the sky have been modeled to derive the intrinsic distributions of space velocity and distance to the CSPN. This has allowed us to infer sound conclusions about their velocity

Table 1
Properties of PNe and Their Jets

PNe and Their Properties						Jets and Their Properties				
Name	PN G	d	a	b	v_{PN}	ID	v_r	θ_s	x	References
		(kpc)	(arcsec)		(km s^{-1})		(km s^{-1})	(arcsec)		
(1)	(2)	(3)	(4)	(5)	(6)	(7)	(8)	(9)	(10)	(11)
IC 4634[a]	000.3+12.2	2.8	4.5	2.9	18	A-A′	19	10.2	2.05	1, 2
						D-D′	19	4.5	0.90	
IC 4776[b]	002.0−13.4	4.4	5.0	2.4	<8	A-B	49.6	4.7	1.34	3, 4
						C-D	84.1	8.1	2.31	
M 1-37	002.6−03.4	14.4	1.4	0.9	11.1	PA = 129°	7.6	2.0	1.16	3
Hb 4[a]	003.1+02.9	2.9	4.2	3.0	21.5	N-S	160	14.6	2.11	5
M 3-15[a]	006.8+04.1	5.5	2.1	1.6	15	E-W	90	5.6	2.13	6, 7
M 2-42[b]	008.2−04.8	9.6	11.2	6.4	15	PA = 0°	15	10.0	2.22	7
M 1-32[c]	011.9+04.2	3.6	5.6	4.9	15	...	180	0.0	0.00	6
HuBi 1	012.2+04.9	3.5	9.3	8.3	22	...	165	0.0	0.00	8
M 2-40	024.1+03.8	5.4	2.7	2.3	17.6	PA = 88°	16.0	4.8	1.64	3
Pe 1-17[b]	024.3−03.3	6.2	7.2	2.2	24	PA = 19°	14.5	6.0	1.20	9
						PA = 50°	5.5	4.8	0.95	
IC 4593[a]	025.3+40.8	1.6	7.8	5.6	15	A-B	2	12.5	1.59	10
						C	1	7.4	0.94	
IC 4846	027.6−09.6	7.1	1.7	1.4	...	A1-A2	48	4.6	1.74	11
						B1-B2	13	3.1	1.18	
NGC 6751[a]	029.2−05.9	2.5	11.8	11.5	41.8	Slit f	31	17.7	1.49	12
PC 19[a]	032.1+07.0	8.3	0.7	0.7	30.5	PA = 28°	35	2.3	0.95	9
M 1-66	032.7−02.0	6.4	1.6	1.4	20.0	PA = 131°	7.0	3.5	1.94	3
NGC 6741[a]	033.8−02.6	3.3	4.1	2.6	23.4	A-B	22.7	8.0	1.78	3
						C	7.3	6.3	1.40	
NGC 6778[d]	034.5−06.7	2.8	10.0	4.5	26	PA = 47°	192	32.0	2.56	13
						PA = 15°	113	34.3	2.74	
NGC 6572	034.6+11.8	1.5	4.2	2.9	14	PA = 15°	8	6.5	1.04	9, 14
						PA = 162°	39	9.0	1.43	
NGC 7009[a]	037.7−34.5	1.3	14.3	5.6	20.8	Slit a	6.5	26.9	1.89	15
NGC 6210[e]	043.1+37.7	2.1	6.6	5.2	34.2	A	19.5	8.4	1.11	3
						B	30.6	4.7	0.62	
						C	29.4	17.6	2.36	
Hen 2-429[b]	048.7+01.9	3.7	3.6	2.8	30.6	PA = 90°	5.9	7.6	2.16	3
Hu 2-1[a]	051.4+09.6	4.2	1.5	0.8	15	C1-C2	54	3.6	1.44	16, 17
						C3-C4	58	3.0	1.20	17
						D	2	5.1	2.00	16, 17
Abell 63[b]	053.9−03.0	2.4	50.0	22.3	17	Polar caps	5.5	142.4	5.70	18
NGC 6891[a]	054.1−12.1	2.9	6.9	6.8	10	A-A′	14	6.0	0.76	14, 19
Necklace[f]	054.2−03.4	4.6	7.3	3.3	28	PA = 34°	54	57.3	6.59	20
Hen 1-1	055.3+02.7	5.7	3.8	2.6	33	PA = 315°	43.5	6.1	1.32	9
K 3-35[c]	056.0+02.0	10.1	2.0	0.6	10	PA = 7°	20	1.8	0.79	21, 22
M 2-48[b]	062.4−00.2	6.4	15.6	7.4	10	B1-B2	7	109.1	9.48	23, 24
BD+30°3639[a]	064.7+05.0	2.2	3.5	3.2	35.5	Slit NS	90	5.5	1.17	25, 26
ETHOS 1[b]	068.1+11.1	8.7	9.7	9.7	55	NW	60	30.0	4.00	27
NGC 6881[a]	074.5+02.1	3.6	2.2	1.4	14	PA = 127°	9	13.8	2.11	28
NGC 6884[a]	082.1+07.0	3.2	3.2	2.9	19	A-A′	22	2.8	0.77	29
						NEK-SWK	36	4.8	1.30	
NGC 6826[a]	083.5+12.7	1.4	13.3	10.5	6	FLIER	44.5	13.9	1.10	15, 30, 31
Hu 1-2[d]	086.5−08.8	5.1	4.8	2.1	32	NW-SE	60	27.6	4.06	32
NGC 6543[e]	096.4+29.9	1.2	13.0	8.3	16	F-F′	32	15.3	1.35	15, 33, 34
						J-J′	39	21.2	1.88	
NGC 7662[a]	106.5−17.6	1.4	14.9	13.2	25	Knot #2	30	17.2	1.25	35
						Jet #22	70	19.4	1.41	
NGC 7354[e]	107.8+02.3	1.3	13.9	10.9	28	A1-A5	5	20.3	1.24	36
KjPn 8[c]	112.5−00.1	...	3.2	2.9	16	A1-A2	220	120	0.91	37
						C1-C2	0	420	3.19	
K 4-47[c]	149.0+04.4	10.4	4.4	1.0	...	PA = 41°	59	3.8	0.90	38
IC 2149	166.1+10.4	2.8	5.4	2.2	24	PA = 67°	0	5.1	0.83	39
J 320	190.3−17.7	5.8	4.5	2.8	16.0	PA = 348°	19.9	9.8	2.39	3
						PA = 338°	34.0	7.8	1.89	
						PA = 306°	24.8	3.7	0.85	
NGC 2392[e]	197.8+17.3	1.4	20.1	20.1	120	PA = 70°	180	22	0.98	40
NGC 1360[c]	220.3−53.9	0.6	229.2	169.2	24	Slit c	76	318	1.27	15, 41

Table 1
(Continued)

PNe and Their Properties						Jets and Their Properties				
Name	PN G	d	a	b	v_{PN}	ID	v_r	θ_s	x	References
		(kpc)	(arcsec)		(km s^{-1})		(km s^{-1})	(arcsec)		
(1)	(2)	(3)	(4)	(5)	(6)	(7)	(8)	(9)	(10)	(11)
						Slit d	81	420	1.68	...
M 1-16[b]	226.7+05.6	6.2	18.2	10.2	...	Slit b	252.5	59	4.74	15, 42
M 3-1[a]	242.6−11.6	4.5	5.0	3.2	24.5	A-B	14.9	12.4	2.39	3
K 1-2[g]	253.5+10.7	3.6	65.2	54.8	25	A3	20.5	16.7	0.56	43
Wray 17-1[b]	258.0−15.7	2.3	46.8	37.8	28	A-B	23.5	32	0.97	43
Wray 17-1[b]						C-D	13	22.5	0.68	
NGC 3242[a]	261.0+32.0	1.0	12.0	7.9	25-30	FLIER	25	15.6	1.26	30, 31
Hen 2-47	285.6−02.7	3.8	2.2	2.1	11.0	PA = 0°	23.5	4.0	1.33	3
						PA = 64°	22.9	3.9	1.28	
Fg 1[b]	290.5+07.9	1.5	32	26.3	36	A-A′	75	110	2.75	44, 45
NGC 3918[e]	294.6+04.7	1.6	8.2	5.8	22.6	A-C	27	23.2	2.72	43
						B	10	13.5	1.59	
Hen 2-90[a]	305.1+01.4	4.9	1.4	1.2	...	Knot h	26	10	7.25	46
MyCn 18[a]	307.5−04.9	2.8	1.8	1.2	24	Knots 2,18	460	49.9	8.32	47
NGC 5307[a]	312.3+10.5	3.2	9.2	5.4	24.5	PA = 0°	6.8	6.6	1.00	48
						PA = 32°	12.0	5.3	0.80	
						PA = 60°	12.1	3.6	0.55	
						PA = 134°	7.3	5.4	0.81	
						PA = 166°	14.7	8.2	1.24	
Hen 2-115	321.3+02.8	5.0	1.4	1.1	13.4	A-B	5.9	2.9	2.59	3
Hen 2-186[a]	336.3−05.6	6.9	1.3	0.8	...	A-B	135	4.5	4.59	38
NGC 6337[b]	349.3−01.1	1.5	28.0	29.1	...	A-B	50	45.8	1.57	38
M 1-26	358.9−00.7	2.1	1.7	1.5	<7	PA = 82°	38.2	3.8	2.76	3
	358.9−00.7					PA = 145°	47.7	3.4	2.51	

Notes. (1) Guerrero et al. (2004), (2) Guerrero et al. (2008), (3) Rechy-García et al. (2019), (4) Sowicka et al. (2017), (5) López et al. (1997), (6) Rechy-García et al. (2017), (7) Akras & López (2012), (8) M. A. Guerrero et al. (2020, in preparation), (9) Guerrero et al. (1999), (10) Corradi et al. (1997), (11) Miranda et al. (2001), (12) Clark et al. (2010), (13) Guerrero & Miranda (2012), (14) Akras & Gonçalves (2016), (15) López et al. (2012), (16) Miranda (1995), (17) Miranda et al. (2001), (18) Mitchell et al. (2007), (19) Guerrero et al. (2000), (20) Corradi et al. (2011), (21) Miranda et al. (2000), (22) Blanco et al. (2014), (23) Vázquez et al. (2000), (24) López-Martín et al. (2002), (25) Bryce & Mellema (1999), (26) Bachiller et al. (2000), (27) Miszalski et al. (2011), (28) Guerrero & Manchado (1998), (29) Miranda et al. (1999), (30) Balick et al. (1987), (31) Balick et al. (1998), (32) Miranda et al. (2012), (33) Miranda & Solf (1992), (34) Reed et al. (1999), (35) Akras et al. (2017), (36) Contreras et al. (2010), (37) López et al. (2002), (38) Corradi et al. (2000), (39) Vázquez et al. (2002), (40) García-Díaz et al. (2012), (41) Goldman et al. (2004), (42) Corradi & Schwarz (1993), (43) Corradi et al. (1999), (44) Lopez et al. (1993), (45) Palmer et al. (1996), (46) Guerrero et al. (2001), (47) O'Connor et al. (2000), and (48) J. S. Rechy-García et al. (2020, in preparation).
[a] *HST* WFPC2-PC F658N [N II] λ6584 image.
[b] No *HST* image available.
[c] Image adopted from the reference in the last column.
[d] NOT ALFOSC [N II] λ6584 image.
[e] *HST* WFPC2-WFC F658N [N II] λ6584 image.
[f] *HST* WFC3/UVIS images.
[g] *HST* WFPC2-WFC F502N [O III] λ5007 image.

and age distributions and compare them to those of their parent PNe.

We describe the selection of the sample and discuss possible selection effects and biases in Section 2. The distributions of the observed radial velocities and projected distances to the CSPNe of the jets are modeled in Section 3 to infer their actual space velocity and distance distributions and investigate their ages. Jets in PNe are found to belong to two different populations with different kinematic properties. In the framework of these results, we discuss different formation mechanisms of jets in PNe and the effects of their interactions with the nebular envelope in Section 4. The main results and conclusions are summarized in Section 5.

2. The Sample of Jets

We have compiled in Table 1 a list of 58 PNe with jets (columns 1 and 2) for which there are available high-dispersion spectroscopic optical observations that provide their kinematic information. Although additional jets are suggested in the optical and near-infrared narrowband images of a larger number of PNe (e.g., Sahai et al. 2011), we have disregarded those with no available kinematic information. Similarly, proto-PNe with jets (e.g., CRL 618 or Hen 3-1475; Borkowski & Harrington 2001; Cox et al. 2003; Lee et al. 2013) have not been included in this study because some of their nebular properties, such as expansion velocity and linear distance to the CSPN, cannot be derived properly. Finally, there is a notorious

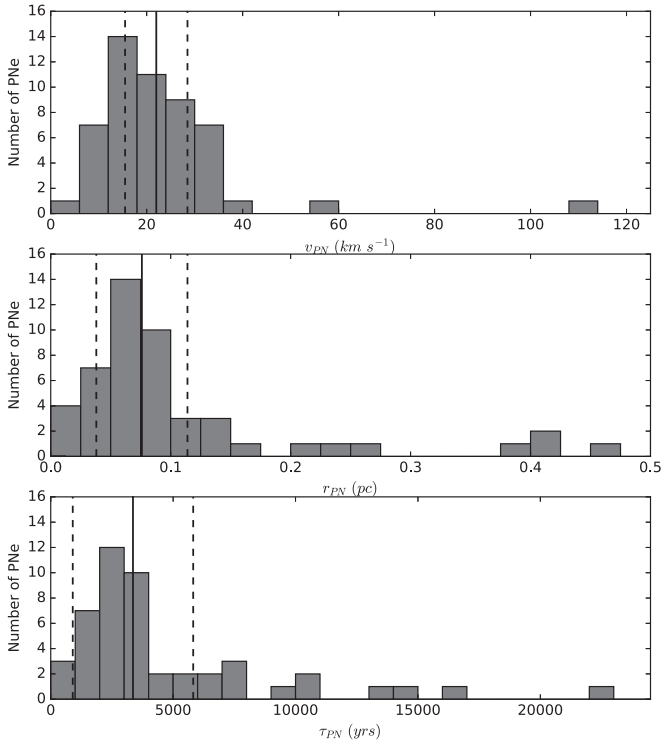

Figure 1. Distributions of the expansion velocity (top), linear radius (middle), and kinematic age (bottom) of the sample of PNe with jets. In each panel, the vertical solid line marks the median value, and the vertical dashed lines the 1σ standard deviation.

sample of bipolar hourglass-shaped PNe that are not included in Table 1 because they do not comply with the morphological and kinematic definition of a jet, even if they present highly collimated lobes (e.g., M 2-9; Clyne et al. 2015).

The final sample of bona fide jets in these 58 sources amounts to 85, as some PNe present several independent sets of such outflows. We next investigate the kinematic and spatial properties of these PNe and their jets.

2.1. Properties of the PNe with Jets

The basic properties (distance, angular size, and expansion velocity) of the PNe with jets are compiled in Table 1. The distances (d) to these sources, listed in column 3, were adopted from Frew et al. (2016) when available, otherwise from Cahn et al. (1992). The angular sizes of their semimajor (a) and semiminor (b) axes are listed in columns 4 and 5, respectively. These were measured mostly in Hα λ6563 *Hubble Space Telescope* (*HST*) WFPC2/PC images. If no available, other *HST* filters or instruments, our own Hα images (for instance, the IAC Morphological Catalog of Northern Galactic PNe; Manchado et al. 1996), or publicly available Hα images (for instance, the University of Hong Kong/Australian Astronomical Observatory/Strasbourg Observatory H-alpha Planetary Nebula Database, HASH PN; Parker et al. 2016) were used for this purpose, as indicated in the footnotes of Table 1. Sizes were estimated using a contour at a 10% level of the peak of the nebular emission. Finally, the expansion velocities of the main nebular shells ($v_{\rm PN}$) as given in the literature are listed in column 6.

In Figure 1, we present the distributions of the expansion velocity ($v_{\rm PN}$); linear nebular radius ($r_{\rm PN}$), computed as

$$r_{\rm PN} = \frac{\sqrt{a^2 + b^2}}{\sqrt{2}} \times d; \quad (1)$$

and kinematic age ($\tau_{\rm PN}$), defined as

$$\tau_{\rm PN} = r_{\rm PN}/v_{\rm PN}, \quad (2)$$

of the PNe in Table 1. These distributions indicate that PNe with jets have median values of 22 ± 7 km s^{-1} for their expansion velocities and 0.076 ± 0.038 pc for their radii. The distribution of the kinematic ages implies a median value of 3400 ± 2500 yr, which points to relatively young PNe. It must be noted, however, that kinematic ages are affected by many dynamical effects that make its use to estimate the PN age (Villaver et al. 2002; Corradi et al. 2007) untrustworthy. Rather, we can use the nebular size of these PNe to estimate their ages, as theoretical models of PN formation show that the nebular size increases with age with varying rates for different initial masses of its progenitor (e.g., Toalá & Arthur 2016). Accordingly, an age between 1000 and 3000 yr can be estimated from the linear size of 0.076 pc.

The relatively small nebular size of PNe with jets suggests that they are found mostly in relatively young PNe and may reveal a bias that hampers the detection of old, evolved outflows that will be discussed in Section 2.3.2.

2.2. Properties of the Jets

2.2.1. Radial Velocities

Columns 7 and 8 of Table 1 provide the identification of the 85 jets with the kinematic information of these 58 PNe and their absolute systemic radial velocities, $|v_{\rm r}^{\rm jet}| \equiv v_{\rm r}$, respectively. The identifications correspond to the names or labels used in the corresponding original references (column 11) or their position angle (PA) on the sky. The systemic radial velocities, i.e., the velocities along the line of sight relative to the systemic velocity of the PN, have been mostly adopted from the literature, as given in the reference listed in column 11. These velocities are typically measured using the [N II] λ6584 emission line rather than the Hα or [O III] λ5007 emission lines, because the smaller thermal width of the [N II] line allows a more accurate determination of the velocity, and the intensity of the [N II] lines is enhanced in these low-excitation features with respect to that of Hα and [O III] (Balick et al. 1994; Gonçalves et al. 2001). In many cases (e.g., M 1-16 and NGC 1360), we have complemented the available kinematic information with measurements we carried out on echelle spectra downloaded from the San Pedro Martir (SPM) Kinematic Catalogue of Galactic PNe (López et al. 2012).

Many jets in PNe exhibit complex kinematic and morphological structures consisting of several components. In particular, a steady increase of velocity with distance to the center of the PN is reported for a significant fraction of them (e.g., Hb 4; Derlopa et al. 2019). In order to use a consistent definition for their radial velocity, we adopted $v_{\rm r}$ to be the largest measured velocity of every single jet in each PN. Different situations can be described. In PNe with a single pair of compact knots confined to one orientation (e.g., NGC 7009), we adopted $v_{\rm r}$ as the semi-difference between their radial velocities. Similar criteria were applied to PNe with two or

more pairs of independent knots along different orientations (e.g., KjPn 8 and NGC 6572) for each pair of jets. On the other hand, some PNe exhibit jets with noticeable changes in orientation and projected velocity. In those cases, wherever the jet was detected as a continuous ejection (e.g., PC 19) or set of discrete knots (e.g., Fg 1), we adopted for v_r the maximum semi-difference between the radial velocities of spatially opposite components. Finally, there are cases where only one single component at one side of the PN is detected or there is no available kinematic information for its counterpart (e.g., feature B in NGC 3918). Here we determined v_r as the difference between the radial velocity of the jet and the PN systemic radial velocity.

2.2.2. Distances of the Jets to the CSPNe

Table 1 also compiles information on the angular distance θ_s from the tip of the jet to the CSPN (column 9). These values have been measured mostly in [N II] images, either in available *HST* or archival images or adopted from the original references (e.g., Fg 1, Palmer et al. 1996).

There are two PNe in our sample, namely M 1-32 and HuBi 1, that can be classified as "spectroscopic bipolar nebulae" (Rechy-García et al. 2017; M. A. Guerrero et al. 2020, in preparation); i.e., their jets have been discovered spectroscopically but are not spatially resolved from the CSPN ($\theta_s = 0$). There are also cases, such as those of MyCn 18 (Bryce et al. 1997) and Hen 2-90 (Sahai & Nyman 2000; Guerrero et al. 2001), for which the jet consists of several knots aligned along the same direction. Following the prescription given above, θ_s was assumed to be the angular distance between the CSPN and the farthest knot (the tip) of the jet.

It can be interesting to refer these angular distances θ_s to the nebular radii, particularly because the detection of a jet may be compromised when its projection falls onto the nebular shell, whose bright emission may outshine it and hinder its detection. The relative distance to the CSPN of the jet with respect to the nebular radius has been defined as

$$x = \theta_s/\theta_{\rm PN-jet}, \quad (3)$$

where $\theta_{\rm PN-jet}$ is the radius of the nebular shell at a 2% level from the peak intensity along the direction of the jet. These values are compiled in column 10 of Table 1.

2.3. Biases

Several biases may hinder the detection of a jet in a PN and affect our sample selection. These are considered below.

2.3.1. Jets Projected onto the PN

Jets in PNe at small inclination angles with the line of sight would be projected onto the main nebular shell, making their detection difficult, as they are embedded in bright nebular emission. Their enhanced brightness in emission lines of low-ionization species and their high degree of collimation, however, make them show up conspicuously on narrowband [N II] images (Manchado et al. 1996), Hα+[N II]-to-[O III] ratio maps (Corradi et al. 1996), or high-dispersion spectroscopic observations (Miranda & Solf 1992; Bryce & Mellema 1999), even if the surrounding nebular emission is much brighter. Still, there can be a lack of detections of jets projected onto the nebular shells of compact and presumably young PNe, as testified by the small number of "spectroscopic bipolar nebulae" and young ($\lesssim$1000 yr) PNe with jets. Spectroscopic searches for high-velocity outflows projected close to CSPNe can improve this situation.

2.3.2. Jets Far from the PN

As jets move away from the main nebulae, they are expected to expand and interact with the circumstellar medium. As they disperse, the detection of low-surface brightness clumps will become difficult. The timescale for jets to disappear will be discussed in Section 3.3, but it is obvious that old jets will be found at large projected distances from their parent PNe, particularly if they also have large expansion velocities and move close to the plane of the sky. As a result, old and fast outflows might be missed in searches using images with a small field of view. Indeed, there is only a small fraction of jets with angular distances to the CSPN greater than 100″ (Fg 1, KjPn 8, M 2-48, and NGC 1360), projected distances to the CSPN greater than 0.5 pc (Ethos 1, Fg 1, Hu 1-2, M 1-16, M 2-48, MyCn 18, NGC 1360, the Necklace Nebula), or relative sizes with respect to their parent nebulae along the direction of the outflow greater than 5 (Hen 2-90, M 2-48, MyCn 18, and the Necklace Nebula). Searches for high-velocity outflows using large-scale narrowband images can improve this situation.

3. Results

The data on the radial velocity and distance to the CSPN of the jets compiled in Table 1 have been plotted in Figure 2. The left panel shows the absolute value of their systemic radial velocities (v_r) versus their relative distances to the CSPN with respect to the nebular radius (x). This panel reveals that most jets are located in the region $x < 2.5$ and $v_r < 100$ km s^{-1}. This region is zoomed in the inset in this plot to reveal a notorious lack of data points for relative distances $x < 0.5$.

Meanwhile, the right panel of Figure 2 compares v_r with the linear distance to the CSPN of the jet projected onto the plane of the sky (r_s). The latter is derived from the distance to the nebula and the angular distance of the jet to the CSPN θ_s as

$$r_s \simeq \theta_s \times d. \quad (4)$$

This panel indicates that most jets have projected distances to the CSPN between 0.05 and 0.3 pc, as emphasized in the inset shown in this panel.

In Figure 2, dots close to the horizontal axes somehow correspond to jets that move close to the plane of the sky, whereas dots at high v_r might be associated with those moving close to the line of sight. Of course, the above statements are to be questioned, as the location of data points in these plots depends on the space velocity, linear distance to the CSPN (i.e., age), and inclination with respect to the line of sight of the jets. The right panel of Figure 2 actually shows that jets with radial velocities $\geqslant$100 km s^{-1} tend to have relatively small ($\lesssim$0.5 pc) projected distances to the CSPN, but the jet of M 1-16. If we assume these small projected distances are due to small inclination angles with the line of sight, it suggests that jets have expansion velocities generally not much higher than 200 km s^{-1}. To allow an investigation of these from a statistical point of view, the occurrences of the v_r, r_s, and x of the jets compiled in Table 1 are plotted in Figure 3. These will be discussed in the next sections.

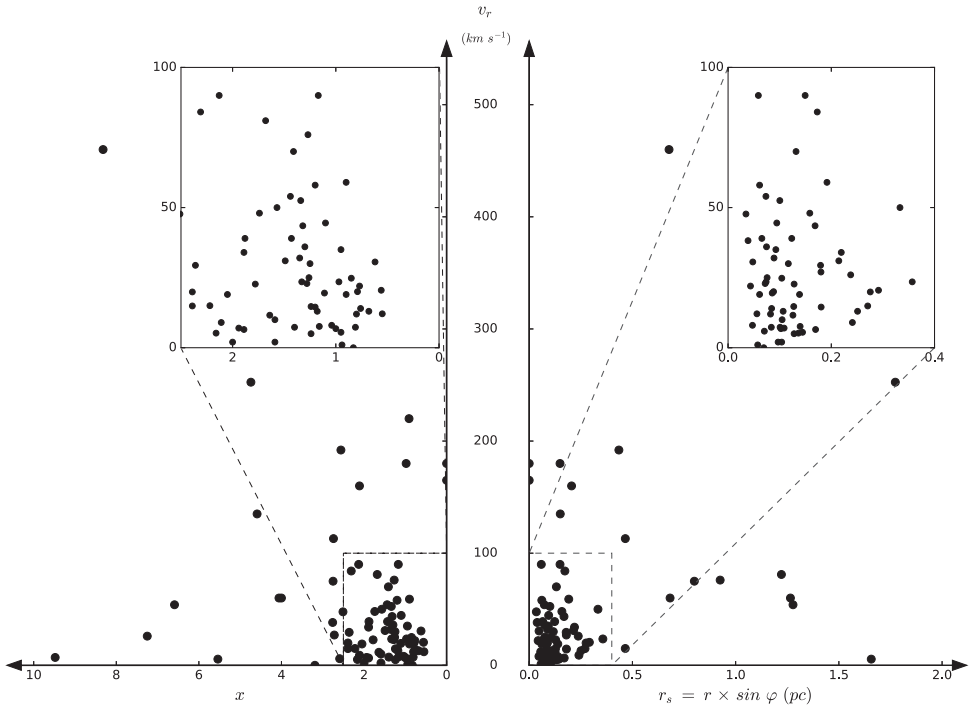

Figure 2. Distribution of the radial velocity of collimated outflows v_r vs. the relative distance to the CSPN with respect to the nebular radius x as defined in Equation (3) (left) and vs. the distance of the collimated outflow to the CSPN projected onto the plane of the sky r_s (right). The innermost regions of these plots are zoomed in the insets.

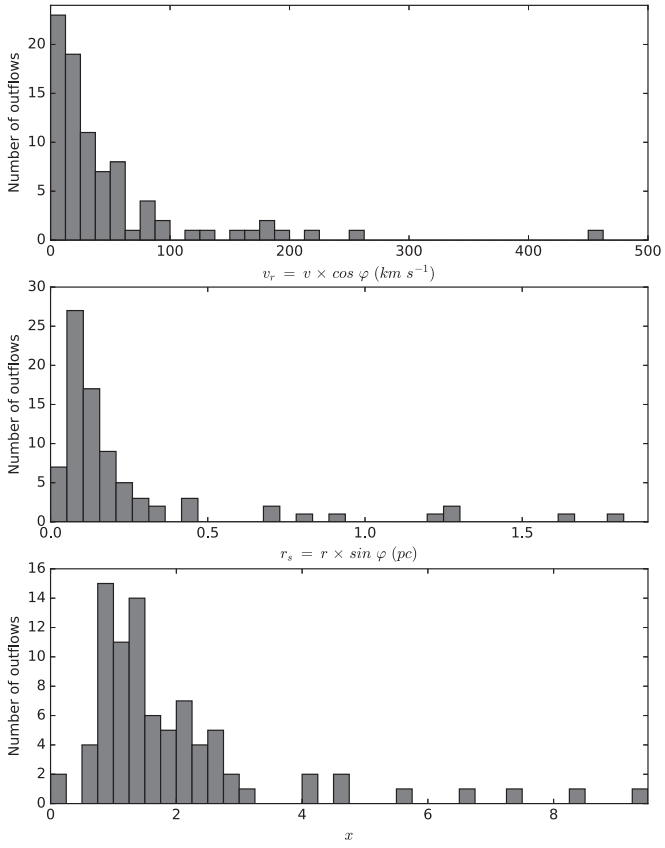

Figure 3. Distributions of the absolute radial velocity $|v_r|$ (top), distance to the CSPN projected onto the plane of the sky r_s (middle), and relative position with respect to the nebular radius x (bottom) of the jets listed in Table 1.

3.1. Distribution of the Absolute Systemic Radial Velocities of Jets

The distribution of v_r in the top panel of Figure 3 shows the number of jets for each radial velocity bin. The v_r distribution declines to velocities $\simeq$100 km s^{-1}, with most jets having radial velocities $\leqslant$100 km s^{-1}. Faster outflows, $v_r \geqslant$ 100 km s^{-1}, are less frequent ($\simeq$12%) and appear spread over a wide range of velocities.

3.1.1. Implications for the Space Velocity Distribution

Let us define φ as the inclination angle with respect to the line of sight of a jet and $v_{\rm exp}^{\rm jet} \equiv v$ its space (i.e., unprojected) velocity. Then, the radial velocity listed in column 8 of Table 1 corresponds to

$$v_r \equiv |v_r^{\rm jet}| = v_{\rm exp}^{\rm jet}\ \times\ |\cos\varphi| \equiv v\ \times\ |\cos\varphi|. \quad (5)$$

Let us define the distribution of the space velocities v as $Q(v)$ and that of the observed absolute radial velocities v_r as $P(v_r)$. It is possible to derive information on $Q(v)$ from $P(v_r)$ on the assumption that the spatial orientation of jets in PNe is isotropic.[4] Let us further assume that the detection of a jet in a PN is not affected by any observational bias, i.e., that the probability of detecting it does not depend on its spatial orientation, projection onto the nebula, or angular distance to the nebula (see Section 2.3). Then, it follows that the space distribution of jets $f(\varphi, \psi)$, with the inclination angle φ from

[4] Corradi et al. (1998) presented convincing arguments that the orientations of axisymmetric PNe in the Galaxy are isotropic, but we must be cautious about extending this to jets in PNe, as their formation mechanism may differ from the general processes involved in the formation of axisymmetric PNe.

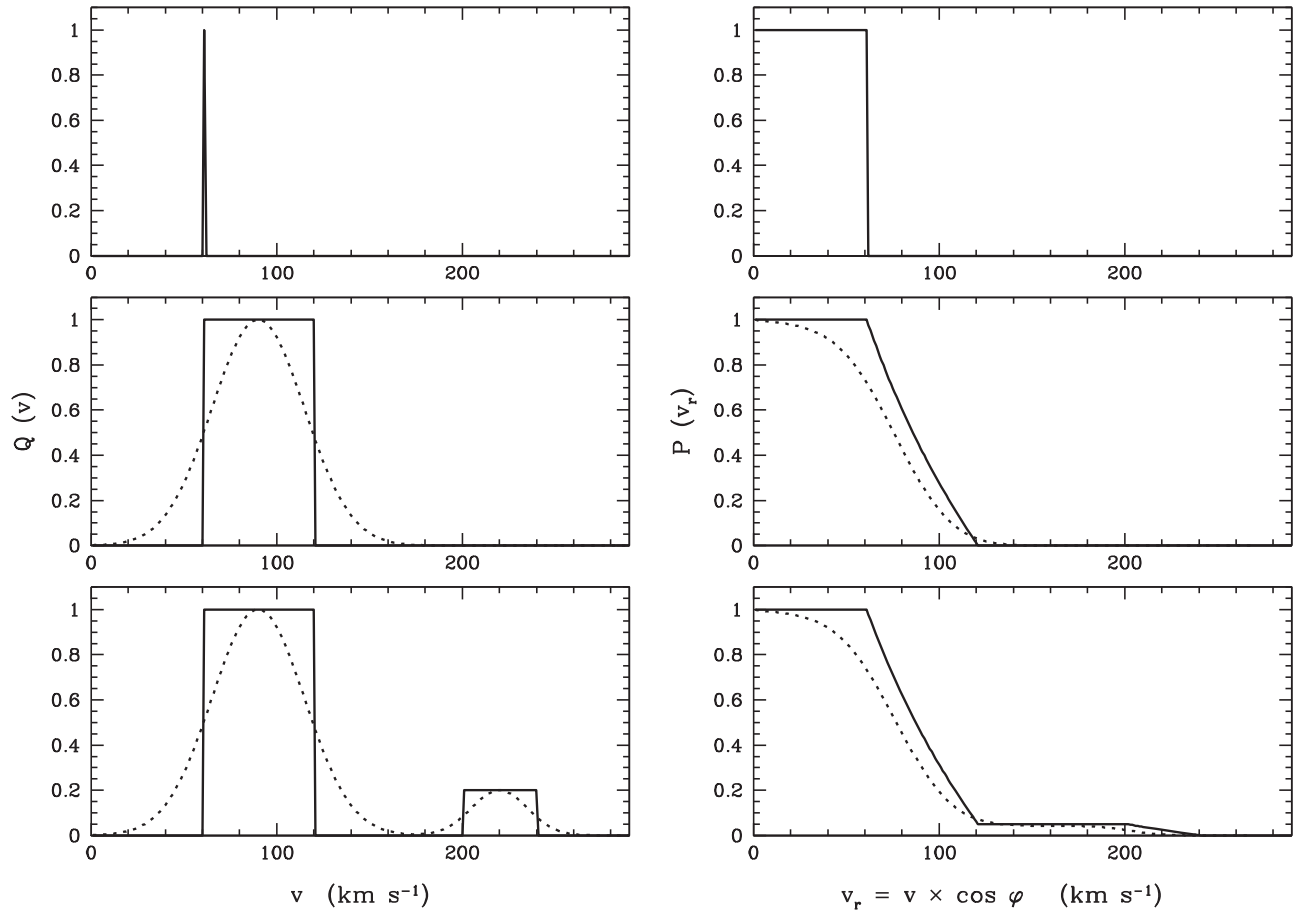

Figure 4. (Left) Different distributions of space velocities $Q(v)$ and (right) their corresponding distribution of radial velocities $P(v_r)$. The $Q(v)$ distributions consist of a single space velocity at $v = 60$ km s^{-1} in the top left panel, a single top-flat (solid line) and Gaussian (dashed line) component centered at $v = 90$ km s^{-1} in the middle left panel, and two top-flat (solid line) and Gaussian (dashed line) components centered at $v = 90$ and 220 km s^{-1} in the bottom left panel. In the latter, the high-velocity component has a lower probability than the low-velocity component.

the line of sight and the azimuthal angle ψ, fulfill the relation

$$\int_0^{+\pi}\int_0^{2\pi} f(\varphi, \psi)d\psi \sin\varphi d\varphi = 1. \quad (6)$$

Since the space distribution of jets does not depend on the spatial direction, it follows that

$$f(\varphi, \psi)\int_0^{\pi}\int_0^{2\pi} d\psi \sin\varphi d\varphi = 4\pi f(\varphi, \psi) \quad (7)$$

for a constant value of the space distribution

$$f(\varphi, \psi) = \frac{1}{4\pi}. \quad (8)$$

Let us suppose that all jets in PNe expanded with identical velocity v_0 (top left panel of Figure 4). The distribution of radial velocities v_r is obtained by considering the above space distribution for each v_r interval. The probability of detecting it with radial velocity $v_1 < v_r < v_2$ is obtained by integrating the isotropic space distribution $f(\varphi, \psi)$ for all of the values of φ and ψ such that the projected radial velocity, as defined by Equation (5), is included in the velocity bin from v_1 to v_2. This can be written as

$$P(v_1\colon v_2) = \int_{\varphi_1}^{\varphi_2}\int_{\psi_1}^{\psi_2} f(\varphi, \psi)d\psi \sin\varphi d\varphi \quad (9)$$

and resolved as

$$P(v_1\colon v_2) = \frac{1}{4\pi}\int_{\varphi_1}^{\varphi_2}\int_{\psi_1}^{\psi_2} d\psi \sin\varphi d\varphi. \quad (10)$$

Since we can write

$$dv_r = -v_0 \sin\varphi d\varphi \;\rightarrow\; \sin\varphi d\varphi = \frac{-dv_r}{v_0}, \quad (11)$$

and because v_r does not depend on the azimuthal angle ψ, the above integral results in

$$P(v_1\colon v_2) = \frac{1}{4\pi}\int_{\varphi_1}^{\varphi_2} 2\pi \sin\varphi d\varphi = \frac{1}{2}\int_{v_2}^{v_1}\frac{-dv_r}{v_0}, \quad (12)$$

which is reduced to

$$P(v_1\colon v_2) = \frac{1}{2}\frac{v_2 - v_1}{v_0}. \quad (13)$$

Actually, since we are considering the absolute value of v_r, we should add both the $P(v_1\colon v_2)$ and $P(-v_2\colon -v_1)$ terms, then resulting in

$$P(|v_1|\colon |v_2|) = P(v_1\colon v_2) + P(-v_2\colon -v_1) = \frac{v_2 - v_1}{v_0}. \quad (14)$$

Equation (14) implies that it is equally probable to detect a jet whose space velocity is v_0 (top left panel of Figure 4) with

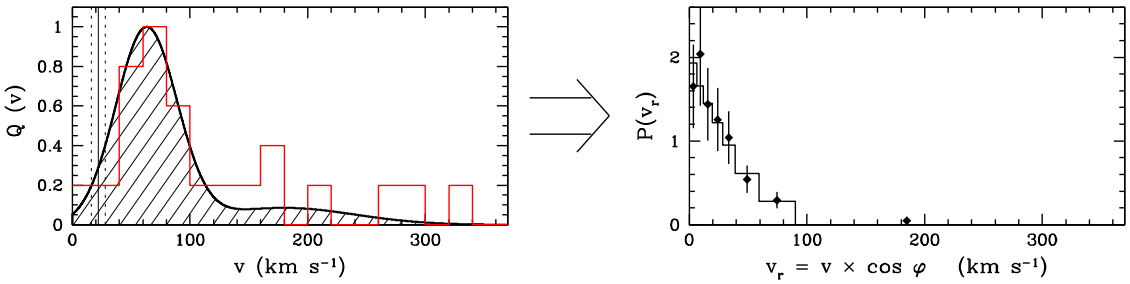

Figure 5. (Left) Best-fit distribution of space velocities $Q(v)$ consisting of a more likely low-velocity and a less likely high-velocity component. The vertical lines mark the median and 1σ standard deviation of the expansion velocity of their parent PNe. The red histogram corresponds to the velocity distribution of jets in PNe whose space velocity has been determined using different methods and assumptions (see Table 2). (Right) Observed distribution of the radial velocities of the jets $P(v_r)$ in our sample (dots) and best-fit synthetic distribution (solid black histogram). The error bars on the observed distribution of v_r are assumed to be the square root of the number of jets per bin. Bin widths are selected to have a similar number of jets per bin.

any value of the absolute radial velocity $v_r < v_0$ (top right panel of the same figure).

Certainly, the $Q(v)$ distribution of velocities can be expected to be different from the single velocity considered above. In such a case, the probability $P(v_r)$ to detect a jet at a radial velocity v_r will be the contribution of the probabilities of all outflows with space velocities $v > v_r$. For instance, for the top-flat $Q(v)$ distribution between two velocities shown in the middle left panel of Figure 4, the observed distribution of v_r would be that shown in the middle right panel of this figure. A very similar result is obtained if using a Gaussian distribution for the space velocity rather than a top-flat distribution, as also shown in the middle panels of Figure 4.

3.1.2. Best-fit Space Velocity Distribution

The shapes of the above distributions do not match that of the observed $P(v_r)$ distribution shown in the top panel of Figure 3. Different initial distributions of space velocity $Q(v)$ have been tested to find that the simplest one producing a distribution of radial velocities $P(v_r)$ similar to that observed consists of two (top-flat or Gaussian) components, one more likely at low velocities to fit the bulk of jets with $v_r \leqslant 100$ km s^{-1} and another less frequent high-velocity component to reproduce the high-velocity tail in $P(v_r)$. Such $Q(v)$ distributions and the resulting $P(v_r)$ distributions are illustrated in the bottom left panel of Figure 4.

Since the detailed shape (top-flat or Gaussian) of these components in $Q(v)$ results in very few differences in the resulting $P(v_r)$ distributions, a space velocity distribution $Q(v)$ represented by two Gaussian components with mean spatial velocities V_1 and V_2, standard deviations σ_1 and σ_2, and probability ratio $\alpha = P_2/P_1$ has been adopted in order to determine the parameters of $Q(v)$ that best fit the observed $P(v_r)$ distribution. The jets in Table 1 have been distributed among eight bins with a similar number of jets ($\simeq$12) but different velocity ranges to allow a statistically unbiased fit. We note, however, that the number of outflows with velocities $\geqslant$100 km s^{-1} is too small (only 10 out of 85) to provide an adequate constraint to the high-velocity component of $Q(v)$. Instead, we have assumed this high-velocity component to have a mean velocity $V_2 = 180$ km s^{-1} and a width $\sigma_2 = 60$ km s^{-1}. The parameters of the low-velocity component of $Q(v)$ and the probability ratio between the two components have been sampled, and a synthetic $P(v_r)$ has been computed for each set of V_1, σ_1, and α. The number of jets per velocity bin in this synthetic distribution is then compared to those in the observed distribution $P(v_r)$ and the difference minimized using a χ^2 optimization algorithm. The best-fit $Q(v)$, with a reduced $\chi^2 \simeq 0.9$, is shown in Figure 5 (left), with the resulting $P(v_r)$ in Figure 5 (right) shown as a solid black histogram. The space velocity of most jets ($\simeq$70%) can be described by the low-velocity Gaussian in the right panel of Figure 5 with a mean velocity of 66 km s^{-1} and a standard deviation of 26 km s^{-1} (FWHM $\simeq$ 60 km s^{-1}).

We noted in Section 1 that the space velocity of the jets of a number of PNe had been derived on the basis of their shock velocity or spatiokinematic models under "reasonable" assumptions for their inclination with the line of sight. These space velocities have been compiled in Table 2, and their velocity distribution is shown as a red histogram in the left panel of Figure 5. There is a noticeable correspondence between the distribution of space velocities $Q(v)$ derived in this section and the distribution as measured in individual PNe, with a prevalence of $\simeq$40% for the detection of faster jets in the latter, most likely revealing that the spatiokinematic modeling or determination of shock velocities is favored for faster jets.

Table 2
Space Velocity of Selected PNe

Name	v (km s^{-1})	Reference
Abell 63	126	Mitchell et al. (2007)
Fg 1	85	Lopez et al. (1993)
Hb 4	220	López et al. (1997)
Hu 1-2	72	Miranda et al. (2001)
Hu 2-1	340	Miranda et al. (2012)
HuBi 1	180	M. A. Guerrero et al. (2020, in preparation)
IC 4634	300	Guerrero et al. (2008)
IC 4846	145	Miranda et al. (2001)
K 1-2	35	Akras & Gonçalves (2016)
Necklace	105	Corradi et al. (2011)
NGC 6572	46, 60	Akras & Gonçalves (2016)
NGC 6751	79	Clark et al. (2010)
NGC 6778	270, 460	Guerrero & Miranda (2012)
NGC 6881	12	Guerrero & Manchado (1998)
NGC 6884	55	Miranda et al. (1999)
NGC 6891	80	Guerrero et al. (2000)
NGC 7354	60	Contreras et al. (2010)
M 1-32	180	Rechy-García et al. (2017)
M 2-42	70	Akras & López (2012)
M 2-48	95	López-Martín et al. (2002)
M 3-15	100	Akras & López (2012)
Wray 17-1	70	Akras & Gonçalves (2016)

3.2. Distribution of the Projected Radial Distances to the CSPN of Jets

The linear distance of a jet to its CSPN (r) is related to its angular distance to the CSPN (θ) and the distance to the PN (d) as

$$r = \tan\theta \times d \simeq \theta \times d. \quad (15)$$

Actually, the parameters directly available to us are their angular and linear distances to the CSPN projected onto the plane of the sky, θ_s and r_s, respectively,

$$r_s \simeq \theta_s \times d = \theta \times d \times \sin\varphi \simeq r \times \sin\varphi, \quad (16)$$

where φ is the inclination angle of the jet with the line of sight as defined in Section 3.1.1. The distribution of r_s in the middle panel of Figure 3 shows the number of jets per bin of distance to the CSPN projected onto the plane of the sky. The distribution of r_s peaks at 0.05–0.15 pc and falls gradually up to 0.4 pc, with only 12 fewer jets (14%) at larger distances than 0.4 pc from the CSPN and even fewer, only seven (8%), at distances smaller than 0.05 pc.

3.2.1. Implications for the Distribution of Linear Distances to the CSPN

Let us define the distribution of the linear distances (i.e., unprojected) of jets to their CSPNe r as $Q(r)$ and that of the observed distribution of distances projected onto the plane of the sky r_s as $P(r_s)$. It is possible to derive information on $Q(r)$ from $P(r_s)$ if we adopt the same assumptions on the isotropic distribution of jets and its unbiased detection. The distribution of sky projected distances r_s is then obtained by considering the space distribution in Equation (8) for each r_s interval. The probability of detecting it at a radial distance $r_1 < r_s < r_2$ is obtained by integrating the isotropic space distribution $f(\varphi, \psi)$ for all values of φ and ψ such that the projected distance r_s as defined by Equation (16) is included in the radial distance bin from r_1 to r_2. This can be written as

$$P(r_1{:}\ r_2) = \int_{\varphi_1}^{\varphi_2}\int_{\psi_1}^{\psi_2} f(\varphi, \psi) d\psi \sin\varphi d\varphi \quad (17)$$

and resolved as

$$P(r_1{:}\ r_2) = \frac{1}{4\pi}\int_{\varphi_1}^{\varphi_2}\int_{\psi_1}^{\psi_2} d\psi \sin\varphi d\varphi. \quad (18)$$

We can write

$$dr_s = r\cos\varphi d\varphi \ \rightarrow\ d\varphi = \frac{dr_s}{r\cos\varphi}, \quad (19)$$

and because r_s does not depend on the azimuthal angle ψ, the above integral results in

$$P(r_1{:}\ r_2) = \frac{1}{4\pi}\int_{\varphi_1}^{\varphi_2} 2\pi\sin\varphi d\varphi = \frac{1}{2r}\int_{r_1}^{r_2}\sin\varphi\frac{dr_s}{\cos\varphi}. \quad (20)$$

Since

$$\frac{\sin\varphi}{\cos\varphi} = \frac{r_s/r}{\sqrt{r^2 - r_s^2}/r} = \frac{r_s}{\sqrt{r^2 - r_s^2}}, \quad (21)$$

the above integral can be solved as

$$P(r_1{:}\ r_2) = \frac{1}{2}\frac{1}{r}\int_{r_1}^{r_2}\frac{r_s}{\sqrt{r^2 - r_s^2}}dr_s = \frac{\sqrt{r^2 - r_1^2}}{r} - \frac{\sqrt{r^2 - r_2^2}}{r}. \quad (22)$$

The behavior of this result is shown in Figure 6 for different distributions $Q(r)$ of the unprojected radial distances r of the jets. If we adopted a single r_0 value for all of them (top left panel of Figure 6), then the expected $P(r_s)$ distribution (top right panel of Figure 6) reveals that it is more likely to detect jets at projected distances close to their actual distances $r_s \simeq r_0$. Like in Section 3.1.1 and Figure 4, we have assumed similar single and double top-flat and Gaussian distributions of $Q(r)$, as shown in the middle and bottom left panels of Figure 6. The resulting $P(r_s)$ distributions are plotted in the corresponding right panels of Figure 6.

3.2.2. Best-fit Model

Like the observed v_r distribution, the observed r_s distribution $P(r_s)$ suggests that the distribution of actual distances $Q(r)$ of jets in PNe needs to be modeled using one component for small ($\leqslant$0.3 pc) values of r_s and a second for large values of r_s. Since there are very few differences between top-flat and Gaussian-shaped distributions, we will assume that $Q(r)$ consists of two Gaussian components with mean values R_1 and R_2, standard deviations σ_1 and σ_2, and probability ratio $\alpha = P_2/P_1$.

The jets in Table 1 have been distributed among eight bins with a similar number of outflows but different widths to allow a statistically unbiased fit. The best-fit parameters have also been obtained using a χ^2 optimization algorithm comparing the synthetic $P(r_s)$ for a space of reasonable parameters and the observed distribution of distances to the CSPN projected onto the plane of the sky shown in the middle panel of Figure 3. The best fit has a reduced $\chi^2 \simeq 0.9$, and the results are shown in Figure 7. The best fit for $P(r_s)$ is achieved with a $Q(r)$ distribution consisting of a Gaussian component with mean radius 0.135 pc and standard deviation 0.055 pc and another with mean radius 0.4 pc and standard deviation 0.4 pc. Most jets ($\simeq$70%) can be ascribed to the first component.

3.3. Age, Time Span, and Formation Time of Jets

The velocity and spatial distributions of jets derived in Sections 3.1.2 and 3.2.2 are not independent. These correlations depend on the distributions of the age and time span of the jets (i.e., their duration before they disperse) and the dynamical effects modifying their kinematics. Therefore, it is possible to estimate the time span (t_{max}) and minimum age (t_{min}) of the jets in our sample by comparing the observed spatial distributions of outflows $P(r_s)$ and that derived from their distribution of space velocities $Q(v)$. The latter has been built using Monte Carlo simulations of a sample of jets whose space velocities are described by the $Q(v)$ distribution derived in Section 3.1.2. In these simulations, the jets have been shot along random directions every year for a total number of 5×10^5 outflows to ensure that the system achieves a stationary regime; i.e., even the lowest-speed outflows could fully evolve until they dissolve after a time span t_{max}.

Different synthetic $P(r_s)$ distributions resulting from simulations exploring a range of values of t_{max} and t_{min} are presented

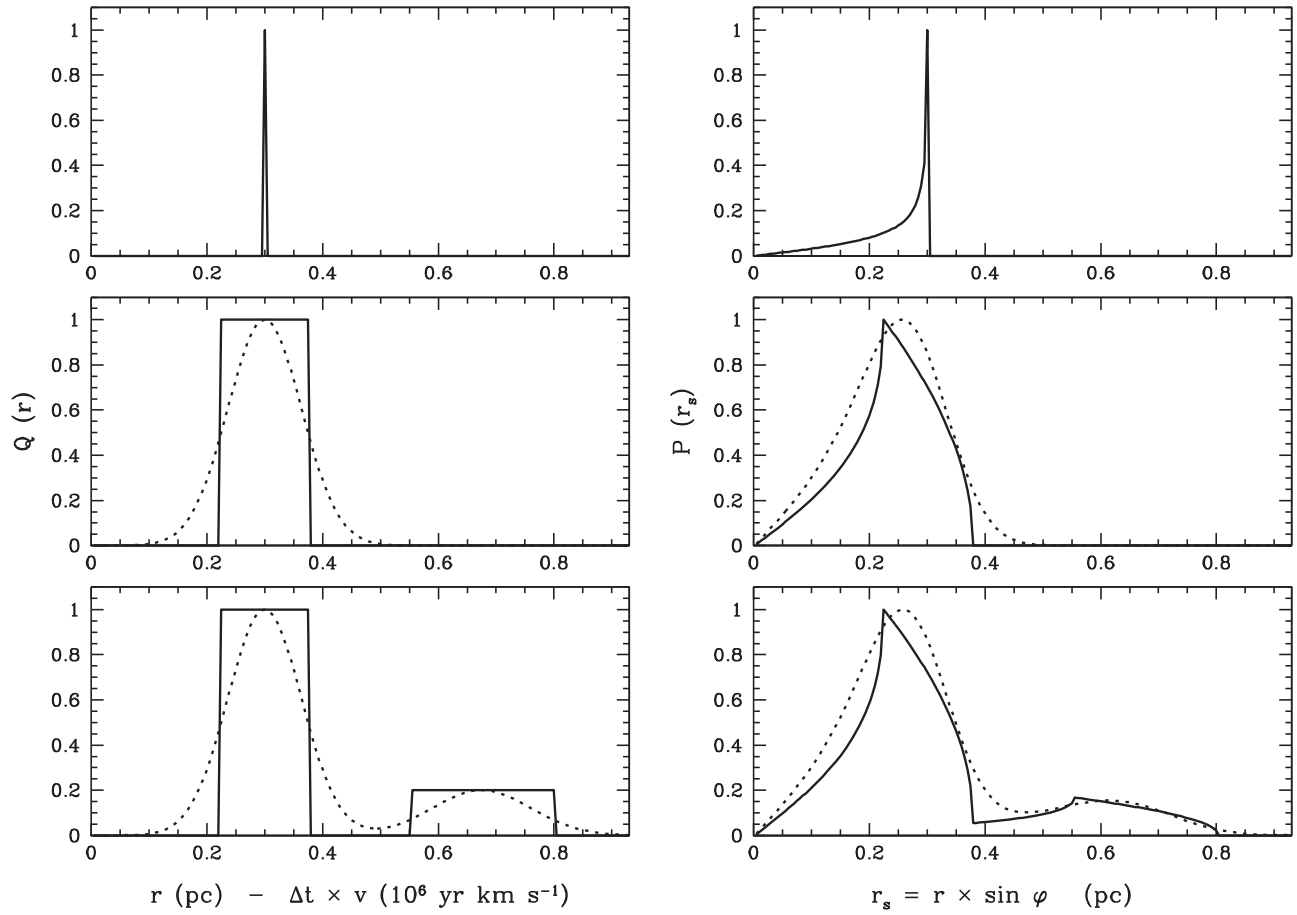

Figure 6. (Left) Different distributions of actual linear distances $Q(r)$ and (right) their corresponding distribution of projected distances onto the plane of the sky $P(r_s)$. The $Q(r)$ distribution consists of a single value of 0.3 pc for r in the top left panel, a single top-flat (solid line) and Gaussian (dashed line) component centered at $r = 0.3$ pc in the middle left panel, and two top-flat (solid line) and Gaussian (dashed line) components centered at $r = 0.3$ and 0.65 pc in the bottom left panel. In the latter, the larger distance component has a lower probability than the smaller distance component.

in Figure 8, together with the observed $P(r_s)$ distribution. An inspection of this figure allows us to constrain the values of t_{max} and t_{min}. The minimum age t_{min} corresponds to the time lapse between the ejection of the jet and the present time and thus, as it increases, the distribution shifts toward larger values of r_s. Synthetic $P(r_s)$ distributions for minimum ages $t_{min} \lesssim 500$ or $\gtrsim$1500 yr cannot reproduce the observed distribution of r_s. On the other hand, the time span t_{max} determines the maximum distance traveled by a jet before it disperses; thus, as it increases, the synthetic distribution broadens and reaches further away from the CSPN. Synthetic $P(r_s)$ distributions for time spans in excess of 3000 yr (shorter than 2000 yr) are broader (narrower) or peak at larger (smaller) linear distances to the CSPN than the observed distribution. The minimum age of 1000 ± 500 yr and time span of 2500 ± 500 yr derived above mark the lower and upper limits, respectively, for the distribution of ages of jets in this sample of PNe.

Unlike studies of jets in individual PNe, where the inclination angles are unknown, the distribution of kinematic ages of the jets in our sample can be derived from their distributions of space velocities $Q(v)$ and actual distances to the CSPNe $Q(r)$. A fraction of $\simeq$70% of the outflows have "low speed," with a mean space velocity of 66 km s^{-1}, and another fraction of $\simeq$70% are "small," with a mean distance to the CSPN of 0.135 pc. Therefore, at least 50% of the outflows in our sample (i.e., 0.70×0.70) have low speed and are small, and their average age is $\sim$2000 yr, with a 1σ width of $\pm$1700 yr according to the 1σ widths of $Q(v)$ and $Q(r)$. Interestingly, a very similar age of $\sim$2200 yr is derived for "high-speed" and "large" outflows adopting an average distance to the CSPN of 0.4 pc and a mean expansion velocity of 180 km s^{-1}. These mean values for the ages of the jets in this sample of PNe are fully consistent with their minimum ages and time spans.

Furthermore, the average age of the jets in this sample and their minimum age and time span are consistent with the age of their parent PNe, which was estimated in Section 2.1 to be 1000–3000 yr. We need to keep in mind that this sample, as described in Section 2, does not include proto-PNe, and then very young outflows are not considered. Including additional jets located near the CSPN in our sample would presumably also add younger PNe, thus reducing both the minimum age t_{min} of the jets and the mean age of their parent PNe. At any rate, this suggests that a noticeable fraction of jets and their parent PNe are mostly coeval; i.e., they formed at about the same time. This is a similar result to that reported by Huggins (2007), who investigated the age of jets and tori in a small sample of proto-PNe and found that their occurrence is almost simultaneous, but it conflicts with results implying that jets are launched a few thousand yr before or after the common-envelope interaction that formed the PN itself (Tocknell et al. 2014). Those results, however, are based on a small sample of only four post-common-envelope PNe that, in spite of the

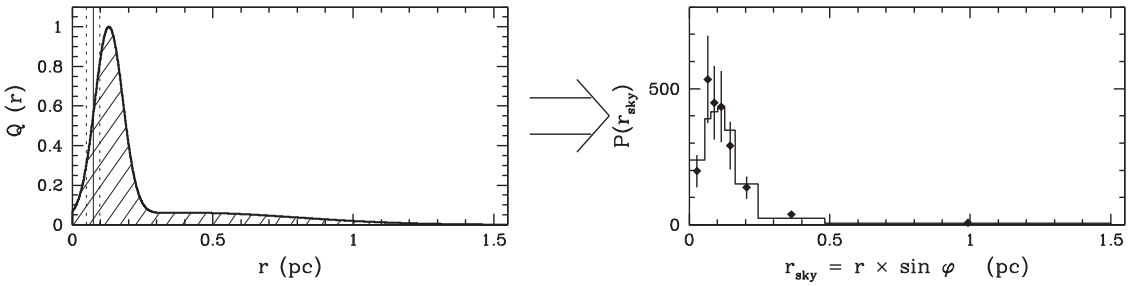

Figure 7. (Left) Best-fit distribution of distances of jets to their CSPNe $Q(r)$ consisting of a more likely closer and a less likely farther component. The vertical lines mark the median and 1σ standard deviation of the linear size of their parent PNe. (Right) Observed distribution of distances projected onto the plane of the sky of the jets $P(r_s)$ in our sample (dots) and best-fit synthetic distribution (black solid histogram). The error bars on the observed distribution of r_s are assumed to be the square root of the number of jets per bin. Bin widths are selected to have a similar number of jets per bin.

addition of a few more recent determinations (Jones & Boffin 2017; Derlopa et al. 2019), are affected by the adoption of kinematic ages as nebular ages (see the discussion of this issue in Section 2.1).

The coeval formation of the jets and their PNe helps us interpret the observed distribution of the relative distance x with respect to the nebular radius along the direction of the jets (bottom panel of Figure 3). Since jets and PNe were formed at the same time, and jets have typical expansion velocities $\simeq$3 times faster than those of their parent PNe, it is unlikely to detect a jet close to the CSPN. Indeed, the small number of jets detected in close proximity to the CSPNe is conspicuous; only the two outflows detected spectroscopically in HuBi 1 and M 1-32 are found below half the nebular radius $x < 0.5$. On the contrary, jets can be expected to be found mostly at a value of x close to three nebular radii, but most have relative distances in the range $0.5 \leqslant x \leqslant 3$, with a notable peak in the bins in the range $0.75 \leqslant x \leqslant 1.5$, and only a small fraction, 20%, are at relative distances at least three times larger than the nebular radius. The large fraction of jets with values of $x \simeq 1$ suggests that the jet was not only ejected at the same time the PN formed, but that jet and PN expanded together as an ensemble.

4. Two Populations of Jets

The analyses of the distributions of the observed radial velocity and projected distances to the CSPN of the PN jets have both yielded bimodal distributions for the space velocity and unprojected distance to the CSPN. The radial distribution of the jets can be inferred from their velocity distribution for reasonable values of their time span and age. Accordingly, jets in PNe can be ascribed to two different populations: most (70%) are "low-speed" (mostly at small distances from the CSPN), with mean space velocities $\sim$66 $\pm$ 26 km s^{-1}, and a smaller fraction (30%) are "high-speed" (mostly at large distances from the CSPN), with space velocities $>$100 km s^{-1}.

Gonçalves et al. (2001) concluded that the low-ionization structures of PNe, of which jets are a prominent group, exhibit a wide range of properties. The bimodal distribution of space velocities of jets in PNe derived in Section 3.1.2 reinforces their suggestion of a different nature among low- and high-velocity outflows. Their distinct kinematic properties most likely imply different launching mechanisms resulting in different prescriptions for their space velocities and/or the way they interact with the nebular envelope. There is a wealth of literature discussing the formation and launch of jets in PNe, but they can be basically split into two major scenarios.

In the first scenario, jets may result from hydrodynamical effects that focus initially isotropic fast winds through oblique shocks associated with a nonspherical low-velocity asymptotic giant branch (AGB) wind (Balick 1987; Balick et al. 1987; Frank et al. 1996). In all of these models, outflows arise at noticeable distances from the CSPN. Typical examples of this collimation process are the FLIERs detected in NGC 6826 and NGC 7009, where the outflows are found at the tips of an elliptical inner shell and connected to these by some filamentary emission (Balick et al. 1987). Very recently, Balick et al. (2020) explored the additional effects of a toroidal magnetic field on tapered (nonisotropic) fast stellar winds and concluded that jets and bullet-like features may form with a range of expansion velocities, depending on the initial injection speed of the fast stellar wind in their models. Somehow related is the collimation of outflows through the interaction of a fast wind with a wrapped disk (Rijkhorst et al. 2005) that result in low-velocity jets, with typical velocities of a few tenths of a km s^{-1}.

More commonly, jets in PNe are accepted to be the result of ballistic ejections, when two compact blobs ("bullets") are symmetrically ejected at high speed from the CSPN (Soker 1990). Magnetic fields have been proposed to be at the origin of this "bipolar" ejection (García-Segura et al. 1999; Steffen et al. 2009), but it is unlikely that their effects become noticeable in single stars (García-Segura et al. 2014). Accordingly, the focus has rather turned into the interaction of the precursor AGB star with a stellar or substellar companion (Livio 1982; Harpaz & Soker 1994; Soker & Livio 1994; Soker 1996), with the possible contribution of magnetic fields emanating from the accretion disk (Frank & Blackman 2004; Dennis et al. 2009). Observational evidence for the existence of circumbinary and accretion disks around dwarf companions (Bujarrabal et al. 2013; Bollen et al. 2017; Ertel et al. 2019) has lent strong support to the formation of jets in binary systems. The outflow would form close to the CSPN, in line with the results of Huggins (2007), who found collimated outflows as close as 9×10^{15} cm (0.003 pc) in a small sample of proto-PNe. The expansion velocity and mass of these bullets will depend on the orbital parameters, accretion rate, and properties of the secondary star. It must be noted that the escape velocity for a 1 $M_{\odot}$ main-sequence companion is much higher (e.g., Bollen et al. 2019) than the typical jet space velocity derived in this work.

The theoretical models for jet formation presented above have difficulty predicting the low-velocity jets mostly detected in PNe, unless ad hoc low velocities are assumed for the stellar wind or the jet is collimated in an accretion disk around a

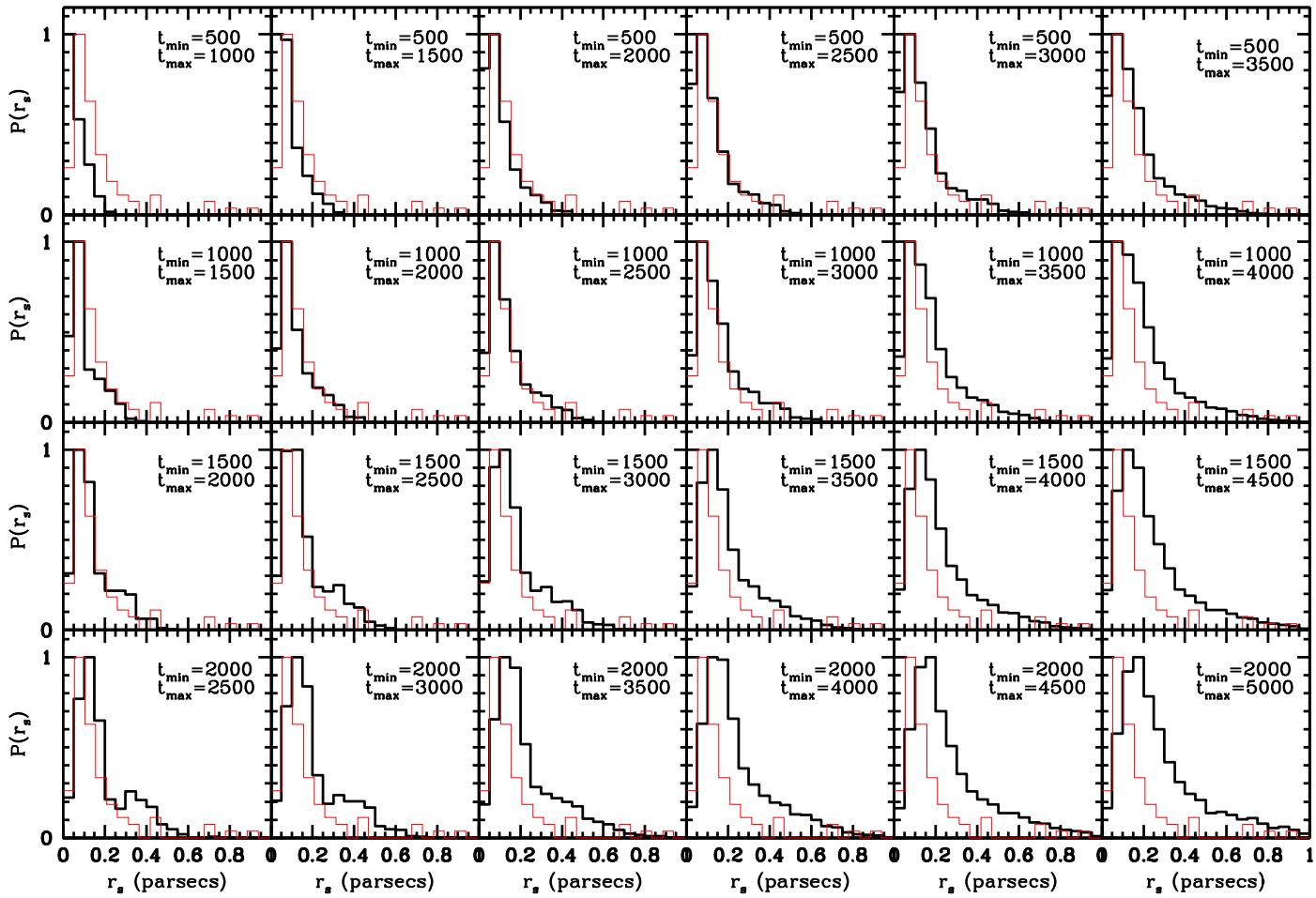

Figure 8. Monte Carlo simulated distributions of $P(r_s)$ for a range of values of the time span (t_{max}) and minimum age (t_{min}) of a population of collimated outflows (black histogram) compared to the observed $P(r_s)$ distribution (red histogram). The best matches between the synthetic and observed $P(r_s)$ distributions are found for 1500 yr $\leqslant t_{max} \leqslant$ 3000 yr and 500 yr $\leqslant t_{min} \leqslant$ 1500 yr.

substellar companion. Alternatively, the interaction of a jet with the previous slow AGB wind can certainly modify its initial velocity, slowing it down. Indeed, among the low-speed component in the $Q(v)$ distribution derived in Section 3.1.2, there is a nonnegligible fraction of jets with expansion velocities similar to or smaller than the median expansion velocities of their parent PNe (Figure 5; left). These can be identified with the low-velocity, low-ionization features described by Perinotto et al. (2004) as SLOWERs or Gonçalves et al. (2001) as jetlike, although it must be noted that those definitions are based on observed radial velocities and thus, unlike the leftmost tail of the $Q(v)$ distribution shown in the left panel of Figure 5, they are subject to notable corrections by their unknown inclination with the line of sight. The interaction between a jet and the nebular envelope is explored below. Two broad cases can be envisaged, depending on whether the outflows can be considered heavy or light (Balick et al. 2019).

Heavy outflows are those with a linear momentum density much larger than the AGB wind, and thus they can be expected to experience very little braking in their interaction with the nebular envelope. Heavy jets may then result in a high-speed population of jets with an expansion velocity in excess of a few hundreds km s^{-1}. Only a handful of PNe present jets with radial velocities >100 km s^{-1}, namely Hb 4, Hen 2-186, HuBi 1, KjPn 8, M 1-16, M 1-32, MyCn 18, NGC 2392, and NGC 6778, although there might certainly be additional high-speed jets that are not directly identified because projection effects decrease their radial velocities. These are presumably the progeny of the young PNe and proto-PNe with the fastest jets, such as CRL 618 (Lee et al. 2013) and Hen 3-1475 (Borkowski & Harrington 2001; Riera et al. 2003), or water fountains such as IRAS 18113−2503 (Orosz et al. 2019). Interestingly, some of the PNe with the fastest jets are known to harbor binary systems (e.g., MyCn 18 and NGC 2392; Miszalski et al. 2018, 2019) or have gone through a common-envelope phase (e.g., NGC 6778; Miszalski et al. 2011).

Light outflows are those whose density is much lower than that of the slow AGB wind, according to the definition introduced by Akashi & Soker (2008). Dynamical effects will certainly distort the space and velocity distributions of light jets produced at the end of the AGB and onset of the proto-PN phases as they interact with the slow AGB wind (Sahai & Trauger 1998). This interaction will slow down their expansion velocities, resulting in a low-speed population of jets. In the most extreme cases of light and wide opening angle outflows, they can get trapped within the nebular envelopes as regions of enhanced density that expand with the PN (Balick et al. 2019). The subsequent interaction of this imprint on the AGB wind with the fast post-AGB wind and strong D-type ionization fronts would shape the PN and may even speed up these features as they are entrained with the nebular envelope (Sahai & Trauger 1998; Soker 2002; Lee & Sahai 2003;

Huarte-Espinosa et al. 2012). These would correspond to the significant fraction of outflows that expand at similar expansion velocities as their parent PNe and whose projected positions onto the main nebular shell suggest that they are embedded within it.

5. Conclusions

We have presented an analysis of the kinematic and spatial properties of a sample of 85 jets detected in 58 PNe. By considering the probability of detecting outflows with different radial velocities and at different radial distances projected onto the plane of the sky, the distributions of their inclination angle–independent space velocity and actual distance to the CSPN have been derived. These happen to be bimodal in both cases. The main component (70%) of the distribution of the space velocity can be described by a Gaussian function with a mean velocity of 66 km s^{-1} and 1σ dispersion of 26 km s^{-1} (or FWHM $\simeq$ 60 km s^{-1}), whereas the secondary (30%) component has a mean velocity of 180 km s^{-1} and 1σ dispersion of 60 km s^{-1} (or FWHM $\simeq$ 140 km s^{-1}). Similarly, the main component (70%) of the distribution of the actual (unprojected) distance to the CSPN can be described by a Gaussian function with a mean distance of 0.135 pc and 1σ dispersion of 0.055 pc (or FWHM $\simeq$ 0.13 pc), whereas the secondary (30%) component has a mean distance of 0.4 pc and 1σ dispersion of 0.4 pc (or FWHM $\simeq$ 1.0 pc).

The comparison of the observed spatial distribution of jets and that derived from their velocity distribution implies that jets are mostly coeval with the formation of their parent PNe and that they disperse in timescales shorter than $\simeq$2500 yr. Since jets are coeval to their parent PNe and last for no more than 2500 yr, PNe that harbor jets are young, with ages $\lesssim$3000 yr.

The low space velocity of jets among a significant fraction of PNe poses notable difficulties for models of jet formation, particularly for those where jets are formed in an accretion disk around a stellar companion. This needs to be linked with the significant number of jets that are found close to the edge of the nebular envelopes, traveling away at velocities similar to the expansion velocities of their parent PNe. These facts support the prevalence among detected jets of "light" outflows that get trapped when interacting with the nebular envelopes, depositing their momentum and energy to actively shape their parent PNe. A possible bias against fast jets at large distances from their PNe cannot be ignored.

The authors acknowledge support from grants AYA 2014-57280-P and PGC2018-102184-B-I00, cofunded with FEDER funds. J.S.R.G. acknowledges financial support from DGAPA-PAPIIT grants IN103117 (PI: Dr. Miriam Peña) and IG100218 (PI: Dr. Pablo F. Velázquez) and scholarship from BECA MIXTA CONACyT-México. This research was motivated a long time ago during an inspiring coffee talk with Dr. Hugo Schwarz. The authors deeply appreciate Dr. Pablo F. Velázquez for his helpful comments, Dr. José A. López for a thorough reading of the manuscript and providing us access to spatiokinematic data from the SPM Kinematic Catalogue of Galactic Planetary Nebulae, and Drs. Noam Soker and B. Balick for their many comments and contributions to the final version of this manuscript.

Based on observations made with the NASA/ESA *Hubble Space Telescope* and obtained from the Hubble Legacy Archive, which is a collaboration between the Space Telescope Science Institute (STScI/NASA), the Space Telescope European Coordinating Facility (ST-ECF/ESA), and the Canadian Astronomy Data Centre (CADC/NRC/CSA). This research has made use of the HASH PN database at hashpn.space, the SPM Kinematic Catalogue of Galactic Planetary Nebulae, NASA's Astrophysics Data System, and the SIMBAD database, operated at CDS, Strasbourg, France.

Facilities: HST(WFPC2, WFC3), NOT(ALFOSC), SPM (2.1 m, MES).

ORCID iDs

Martín A. Guerrero https://orcid.org/0000-0002-7759-106X
Jackeline Suzett Rechy-García https://orcid.org/0000-0002-0121-2537
Roberto Ortiz https://orcid.org/0000-0002-0084-8373

References

Akashi, M., & Soker, N. 2008, MNRAS, 391, 1063
Akras, S., & Gonçalves, D. R. 2016, MNRAS, 455, 93
Akras, S., Gonçalves, D. R., & Ramos-Larios, G. 2017, MNRAS, 465, 1289
Akras, S., & López, J. A. 2012, MNRAS, 425, 2197
Alcolea, J., Bujarrabal, V., Castro-Carrizo, A., et al. 2000, in ASP Conf. Ser. 199, Asymmetrical Planetary Nebulae II: From Origins to Microstructures, ed. J. H. Kastner, N. Soker, & S. Rapport (San Francisco, CA: ASP), 347
Bachiller, R., Forveille, T., Huggins, P. J., Cox, P., & Maillard, J. P. 2000, A&A, 353, L5
Balick, B. 1987, AJ, 94, 671
Balick, B., Alexander, J., Hajian, A. R., et al. 1998, AJ, 116, 360
Balick, B., Frank, A., & Liu, B. 2019, ApJ, 877, 30
Balick, B., Frank, A., & Liu, B. 2020, ApJ, 889, 13
Balick, B., Perinotto, M., Maccioni, A., Terzian, Y., & Hajian, A. 1994, ApJ, 424, 800
Balick, B., Preston, H. L., & Icke, V. 1987, AJ, 94, 1641
Balick, B., Rugers, M., Terzian, Y., et al. 1993, ApJ, 411, 778
Blanco, M. W., Guerrero, M. A., Miranda, L. F., Lagadec, E., & Suárez, O. 2014, A&A, 561, A81
Bollen, D., Kamath, D., Van Winckel, H., et al. 2019, A&A, 631, A53
Bollen, D., Van Winckel, H., & Kamath, D. 2017, A&A, 607, A60
Bond, H. E., & Livio, M. 1990, ApJ, 355, 568
Borkowski, K. J., & Harrington, J. P. 2001, ApJ, 550, 778
Bryce, M., López, J. A., Holloway, A. J., & Meaburn, J. 1997, ApJ, 487L, 161
Bryce, M., & Mellema, G. 1999, MNRAS, 309, 731
Bujarrabal, V., Alcolea, J., Van Winckel, H., et al. 2013, A&A, 557, A104
Cahn, J. H., Kaler, J. B., & Stanghellini, L. 1992, A&AS, 94, 399
Clark, D. M., García-Díaz, M. T., López, J. A., Steffen, W. G., & Richer, M. G. 2010, ApJ, 722, 1260
Clyne, N., Akras, S., Steffen, W., et al. 2015, A&A, 582, A60
Contreras, M. E., Vázquez, R., Miranda, L. F., et al. 2010, AJ, 139, 1426
Corradi, R. L. M., Aznar, R., & Mampaso, A. 1998, MNRAS, 297, 617
Corradi, R. L. M., Gonçalves, D. R., Villaver, E., et al. 2000, ApJ, 535, 823
Corradi, R. L. M., Guerrero, M. A., Manchado, A., & Mampaso, A. 1997, NewA, 2, 461
Corradi, R. L. M., Manso, R., Mampaso, A., & Schwarz, H. E. 1996, A&A, 313, 913
Corradi, R. L. M., Perinotto, M., Villaver, E., Mampaso, A., & Gonçalves, D. R. 1999, ApJ, 523, 721
Corradi, R. L. M., Sabin, L., Miszalski, B., et al. 2011, MNRAS, 410, 1349
Corradi, R. L. M., & Schwarz, H. E. 1993, A&A, 278, 247
Corradi, R. L. M., Steffen, M., Schönberner, D., et al. 2007, A&A, 474, 529
Cox, P., Huggins, P. J., Maillard, J.-P., et al. 2003, ApJL, 586, L87
Cox, P., Lucas, R., Huggins, P. J., et al. 2000, A&A, 353, L25
Dennis, T. J., Frank, A., Blackman, E. G., et al. 2009, ApJ, 707, 1485
Derlopa, S., Akras, S., Boumis, P., et al. 2019, MNRAS, 484, 3746
Ertel, S., Kamath, D., Hillen, M., et al. 2019, AJ, 157, 110
Frank, A., Balick, B., & Livio, M. 1996, ApJL, 471, L53
Frank, A., & Blackman, E. G. 2004, ApJ, 614, 737
Frew, D. J., Parker, Q. A., & Bojičić, I. S. 2016, MNRAS, 455, 1459
García-Díaz, M. T., López, J. A., Steffen, W., & Richer, M. G. 2012, ApJ, 761, 172
García-Segura, G. 1997, ApJL, 489, L189
García-Segura, G., Langer, N., Różyczka, M., et al. 1999, ApJ, 517, 767

García-Segura, G., Villaver, E., Langer, N., Yoon, S.-C., & Manchado, A. 2014, ApJ, 783, 74
Gieseking, F., Becker, I., & Solf, J. 1985, ApJL, 295, L17
Goldman, D. B., Guerrero, M. A., Chu, Y.-H., & Gruendl, R. A. 2004, AJ, 128, 1711
Gonçalves, D. R., Corradi, R. L. M., & Mampaso, A. 2001, ApJ, 547, 302
Guerrero, M. A., & Manchado, A. 1998, ApJ, 508, 262
Guerrero, M. A., & Miranda, L. F. 2012, A&A, 539, A47
Guerrero, M. A., Miranda, L. F., & Chu, Y.-H. 2004, in ASP Conf. Ser. 313, Asymmetrical Planetary Nebulae III: Winds, Structure and the Thunderbird, ed. M. Meixner et al. (San Francisco, CA: ASP), 30
Guerrero, M. A., Miranda, L. F., Chu, Y.-H., Rodríguez, M., & Williams, R. M. 2001, ApJ, 563, 883
Guerrero, M. A., Miranda, L. F., Manchado, A., & Vázquez, R. 2000, MNRAS, 313, 1
Guerrero, M. A., Miranda, L. F., Riera, A., et al. 2008, ApJ, 683, 272
Guerrero, M. A., Vázquez, R., & López, J. A. 1999, AJ, 117, 967
Harpaz, A., & Soker, N. 1994, MNRAS, 270, 734
Harrington, J. P., Lame, N. J., White, S. M., & Borkowski, K. J. 1997, AJ, 113, 2147
Hartigan, P., Raymond, J, & Hartmann, L. 1987, ApJ, 316, 323
Huarte-Espinosa, M., Frank, A., Balick, B., et al. 2012, MNRAS, 424, 2055
Huggins, P. J. 2007, ApJ, 663, 342
Jones, D., & Boffin, H. M. J. 2017, NatAs, 1, 0117
Lee, C.-F., & Sahai, R. 2003, ApJ, 586, 319
Lee, C.-F., Sahai, R., Sánchez Contreras, C., Huang, P.-S., & Hao Tay, J. J. 2013, ApJ, 777, 37
Livio, M. 1982, A&A, 105, 37
Livio, M. 1999, PhR, 311, 225
López, J. A., Meaburn, J., Bryce, M., & Rodríguez, L. F. 1997, ApJ, 475, 705
Lopez, J. A., Meaburn, J., & Palmer, J. W. 1993, ApJL, 415, L135
López, J. A., Richer, M. G., García-Díaz, M. T., et al. 2012, RMxAA, 48, 3
López, J. A., Rodríguez, L. F., Meaburn, J., et al. 2002, in Revista Mexicana De Astronomia Y Astrofisica Conf. Ser. 12, Ionized Gaseous Nebulae, a Conference to Celebrate the 60th Birthdays of Silvia Torres-Peimbert and Manuel Peimbert (Mexico, Mexico City), 123
López, J. A., Steffen, W., & Meaburn, J. 1997, ApJ, 485, 697
López, J. A., Vazquez, R., & Rodriguez, L. F. 1995, ApJL, 455, L63
López-Martín, L., López, J. A., Esteban, C., et al. 2002, A&A, 388, 652
Manchado, A., Guerrero, M. A., Stanghellini, L., & Serra-Ricart, M. 1996, The IAC Morphological Catalog of Northern Galactic Planetary Nebulae (La Laguna, Spain: IAC Publications)
Miranda, L. F. 1995, A&A, 304, 531
Miranda, L. F., Blanco, M., Guerrero, M. A., & Riera, A. 2012, MNRAS, 421, 1661
Miranda, L. F., Fernández, M., Alcalá, J. M., et al. 2000, MNRAS, 311, 748
Miranda, L. F., Guerrero, M. A., & Torrelles, J. M. 1999, AJ, 117, 1421
Miranda, L. F., Guerrero, M. A., & Torrelles, J. M. 2001, MNRAS, 322, 195
Miranda, L. F., & Solf, J. 1992, A&A, 260, 397
Miranda, L. F., Torrelles, J. M., Guerrero, M. A., Vázquez, R., & Gómez, Y. 2001, MNRAS, 321, 487
Miranda, L. F., Vázquez, R., Corradi, R. L. M., et al. 1999, ApJ, 520, 714
Miszalski, B., Corradi, R. L. M., Boffin, H. M. J., et al. 2011, MNRAS, 413, 1264
Miszalski, B., Jones, D., Rodríguez-Gil, P., et al. 2011, A&A, 531, A158
Miszalski, B., Manick, R., Mikołajewska, J., Van Winckel, H., & Iłkiewicz, K. 2018, PASA, 35, e027
Miszalski, B., Manick, R., Van Winckel, H., & Escorza, A. 2019, PASA, 36, e018
Mitchell, D. L., Pollacco, D., O'Brien, T. J., et al. 2007, MNRAS, 374, 1404
Morris, M. 1987, PASP, 99, 1115
O'Connor, J. A., Redman, M. P., Holloway, A. J., et al. 2000, ApJ, 531, 336
Orosz, G., Gómez, J. F., Imai, H., et al. 2019, MNRAS, 482, L40
Palmer, J. W., López, J. A., Meaburn, J., & Lloyd, H. M. 1996, A&A, 307, 225
Parker, Q. A., Bojičić, I. S., & Frew, D. J. 2016, JPhCS, 728, 032008
Perinotto, M., Patriarchi, P., Balick, B., et al. 2004, A&A, 422, 963
Rechy-García, J. S., Guerrero, M. A., Duarte Puertas, S., et al. 2019, MNRAS, in press
Rechy-García, J. S., Velázquez, P. F., Peña, M., & Raga, A. C. 2017, MNRAS, 464, 2318
Reed, D. S., Balick, B., Hajian, A. R., et al. 1999, AJ, 118, 2430
Riera, A., García-Lario, P., & Manchado, A. 2003, A&A, 401, 1039
Rijkhorst, E.-J., Mellema, G., & Icke, V. 2005, A&A, 444, 849
Sahai, R., & Nyman, L.-Å. 2000, ApJL, 538, L145
Sahai, R., Morris, M. R., & Villar, G. G. 2011, AJ, 141, 134
Sahai, R., & Trauger, J. T. 1998, AJ, 116, 1357
Soker, N. 1990, AJ, 99, 1869
Soker, N. 1996, ApJ, 468, 774
Soker, N. 2002, ApJ, 568, 726
Soker, N., & Livio, M. 1994, ApJ, 421, 219
Sowicka, P., Jones, D., Corradi, R. L. M., et al. 2017, MNRAS, 471, 3529
Stanghellini, L., Villaver, E., Manchado, A., & Guerrero, M. A. 2002, ApJ, 576, 285
Steffen, W., García-Segura, G., & Koning, N. 2009, ApJ, 691, 696
Toalá, J. A., & Arthur, S. J. 2016, MNRAS, 463, 4438
Tocknell, J., De Marco, O., & Wardle, M. 2014, MNRAS, 439, 2014
Vázquez, R., López-Martín, L., Miranda, L. F., et al. 2000, A&A, 357, 1031
Vázquez, R., Miranda, L. F., Torrelles, J. M., et al. 2002, ApJ, 576, 860
Villaver, E., Manchado, A., & García-Segura, G. 2002, ApJ, 581, 1204